PHYSICAL REVIEW MATERIALS **2**, 013402 (2018)

Molecular dynamics studies of InGaN growth on nonpolar $(11\bar{2}0)$ GaN surfaces

K. Chu,[1] J. Gruber,[2] X. W. Zhou,[1,*] R. E. Jones,[1] S. R. Lee,[3] and G. J. Tucker[2]
[1]*Mechanics of Materials Department, Sandia National Laboratories, Livermore, California 94550, USA*
[2]*Mechanical Engineering Department, Colorado School of Mines, Golden, Colorado 80401, USA*
[3]*Advanced Materials Sciences Department, Sandia National Laboratories, Albuquerque, New Mexico 87123, USA*

(Received 10 October 2017; published 31 January 2018)

We have performed direct molecular dynamics (MD) simulations of heteroepitaxial vapor deposition of $In_xGa_{1-x}N$ films on nonpolar $(11\bar{2}0)$ wurtzite-GaN surfaces to investigate strain relaxation by misfit-dislocation formation. The simulated growth is conducted on an atypically large scale by sequentially injecting nearly a million individual vapor-phase atoms towards a fixed GaN substrate. We apply time-and-position-dependent boundary constraints to affect the appropriate environments for the vapor phase, the near-surface solid phase, and the bulklike regions of the growing layer. The simulations employ a newly optimized Stillinger-Weber In-Ga-N system interatomic potential wherein multiple binary and ternary structures are included in the underlying density-functional theory and experimental training sets to improve the treatment of the In-Ga-N related interactions. To examine the effect of growth conditions, we study a matrix of 63 different MD-growth simulations spanning seven $In_xGa_{1-x}N$-alloy compositions ranging from $x = 0.0$ to $x = 0.8$ and nine growth temperatures above half the simulated melt temperature. We found a composition dependent temperature range where all kinetically trapped defects were eliminated, leaving only quasiequilibrium misfit and threading dislocations present in the simulated films. Based on the MD results obtained in this temperature range, we observe the formation of interfacial misfit and threading dislocation arrays with morphologies strikingly close to those seen in experiments. In addition, we compare the MD-observed thickness-dependent onset of misfit-dislocation formation to continuum-elasticity-theory models of the critical thickness and find reasonably good agreement. Finally, we use the three-dimensional atomistic details uniquely available in the MD-growth histories to directly observe the nucleation of dislocations at surface pits in the evolving free surface.

DOI: 10.1103/PhysRevMaterials.2.013402

I. INTRODUCTION

Due to its energy efficiency, solid-state lighting (SSL) has begun to broadly replace conventional light sources [1–5]; however, the “green gap” [6] in SSL efficiency remains a major hurdle in this technological transformation. To achieve white light with a suitable spectrum, high-efficiency red, green, and blue (RGB) light emitters are needed. While high efficiencies have been achieved for blue and red light, the emission efficiency for green-to-yellow light needed for the color-mixing approach is significantly lower and phosphor-based down-conversion is used as a less efficient stop gap.

AlGaInP-alloy films have been the primary material for red light emission at longer wavelengths (570 to 680 nm), and $In_xGa_{1-x}N$-alloy films have been used for blue light emission (<530 nm) [7]. In AlGaInP there is a fundamental barrier to pushing the emission wavelength towards green by increasing the Al content since the increase in Al concentration is associated with a transition from a direct energy band gap. $In_xGa_{1-x}N$, on the other hand, can be tuned to the green spectral range and beyond by increasing the indium content without incurring an indirect band gap. Despite extensive studies, however, an abrupt reduction in the blue-green (>500 nm) emission efficiency of $In_xGa_{1-x}N$ films where indium content is increased to $x > 0.2{-}0.3$ [8] remains.

The drop in quantum efficiency of these higher indium content $In_xGa_{1-x}N$ films have been attributed primarily to three different mechanisms [9–12]: (a) large lattice mismatch between $In_xGa_{1-x}N$ and underlying GaN substrates leads to high dislocation densities; (b) thermodynamically driven phase separation leads to composition inhomogeneity; and (c) internal piezoelectric and spontaneous polarization fields lead to local separation of the electrons and holes. Regarding the lattice mismatch effect, experiments indicated that increasing indium content promotes strain relaxation through defect formation [13,14]. Furthermore, there exists a critical layer thickness, above which defects begin to form and the optical properties deteriorate [15,16]. As a result, tremendous efforts have been made to understand the strain relaxation between $In_xGa_{1-x}N$ and GaN due to misfit dislocation formation through both theoretical [17,18] and experimental [19–23] developments since GaN is currently the most feasible substrate for growing $In_xGa_{1-x}N$ films. Due to the challenges in directly visualizing the formation process of the three-dimensional network of misfit dislocations, previous theory necessarily involved numerous assumptions that have yet to be validated. Molecular dynamics (MD) simulation of growth of $In_xGa_{1-x}N$ films on GaN substrates provides an effective theoretical means to validate these assumptions.

Recently we performed extensive MD simulations of growth of $In_xGa_{1-x}N$ films on polar (0001) GaN surfaces [24]. The simulations provided substantial insight into formation mechanisms of various defects including stacking

---

[*] Corresponding author: xzhou@sandia.gov

faults/polymorphism, associated domain boundaries, surface roughness, dislocations, and voids; however, strain relaxation and misfit dislocation formation were not studied due to the interference of these other defects. In the present work we perform extensive MD simulations of growth of $\mathrm{In}_x\mathrm{Ga}_{1-x}\mathrm{N}$ films on nonpolar $(11\bar{2}0)$ GaN surfaces that eliminate the formation of many other defects [24] so that we can reveal the strain relaxation and misfit dislocation formation mechanisms.

II. METHODS

A. Interatomic potential

As in the previous simulations of $\mathrm{In}_x\mathrm{Ga}_{1-x}\mathrm{N}$ growth on polar (0001) GaN [24], we use a Stillinger-Weber (SW) [25] type In-Ga-N potential [26,27] for our simulations. This potential has been developed to capture (a) the lowest energies for the equilibrium wurtzite (wz) phase of both GaN and InN, (b) the experimental or density-functional theory (when experimental data are unavailable) cohesive energies for elements (Ga, In, N), (c) the experimental atomic volumes and cohesive energies for compounds (GaN and InN), and (d) the crystalline growth of both wz and zinc-blende (zb) phases of alloyed $\mathrm{In}_x\mathrm{Ga}_{1-x}\mathrm{N}$ films during molecular dynamics (MD) simulations. Specifically, the capacity for crystalline growth validates the stability of the correct $\mathrm{In}_x\mathrm{Ga}_{1-x}\mathrm{N}$ phases over other configurations [28], which is not always the case with literature potentials. However, the SW potential is constrained by its formulation to have zero stacking fault energy. This is a fair, perhaps even a good, approximation since first-principle calculations indicate that the energy difference between wz and zb phases is small (∼10 meV/atom) for both InN and GaN [29].

The lattice constant of the wurtzite $\mathrm{In}_x\mathrm{Ga}_{1-x}\mathrm{N}$ alloy as a function of temperature and composition has been calculated using time-averaged MD simulations, and the results were provided previously [24]. However, we found that the composition defined in the previous expression was inadvertently doubled. The corrected expressions for lattice constants (in angstroms) are: $a = 3.202\,[1 + 6.208 \times 10^{-6}\,(T - 1800) + 0.1086\,x_{\mathrm{In}}]$ and $c = 5.230\,[1 + 5.390 \times 10^{-6}\,(T - 1800) + 0.1076\,x_{\mathrm{In}}]$. Note that in this paper, sometimes we use x_{In} instead of x (as in the $\mathrm{In}_x\mathrm{Ga}_{1-x}\mathrm{N}$ chemical formula) to avoid confusion with the coordinate direction x.

As a further check of the validity of the potential, we calculated the dislocation core energy E_c by fitting dislocation energy as a function of dislocation spacing as detailed in Refs. [30,31]. Assuming a core radius of 8.5 Å, we obtained $E_c = 1.63\,\mathrm{eV/Å}$ for wurtzite GaN and $1.23\,\mathrm{eV/Å}$ for wurtzite InN with negligible statistical error in the fit to the continuum solution. A relation of the shear modulus G and Poisson's ratio ν was obtained as a by-product of the fitting: $2G/(1 - \nu) = 2.198\,\mathrm{eV/Å^3}$ (GaN) and $1.455\,\mathrm{(InN)}\,\mathrm{eV/Å^3}$. The wz GaN core energy is comparable to the $2.19\,\mathrm{eV/Å}$ estimated with density-functional theory in Refs. [32,33] for the same core radius.

B. MD growth algorithm

A procedure like that of previous work [24] was used to simulate the $\mathrm{In}_x\mathrm{Ga}_{1-x}\mathrm{N}$ growth on nonpolar $(11\bar{2}0)$ GaN substrates. As shown by the underlying dark-gray regions in Fig. 1 and subsequent similar figures, the initial wurtzite-GaN substrates contain 84 $(1\bar{1}00)$ planes in the x direction, 12 $(11\bar{2}0)$ planes in the y direction, and 82 (0002) or equivalently 41 (0001) planes in the z direction. The relatively large substrate choice enables a large simulated-growth system where the total number of atoms reaches ∼0.8 million after the completion of a simulated growth to $\mathrm{In}_x\mathrm{Ga}_{1-x}\mathrm{N}$-alloy thicknesses of ∼16−20 nm. The initial lattice constants of the crystals were set to the 0 K values determined from molecular statics (MS) simulations [26]. Referring to Fig. 1, periodic boundary conditions were used in the lateral directions (x and z), whereas a nonperiodic boundary condition was used in the growth direction (y) to allow for a free surface. Growth was simulated by injecting In, Ga, and N adatoms towards the top y surface from random locations far above the surface. The specific injection of an In, Ga, or N atom at any instant was randomized subject to overall compositional and growth-rate constraints. Initial far field adatoms have a kinetic energy $E_i = 0.1$ eV and are moving perpendicular to the surface, and the prescribed growth rate is $R = 0.4 - 0.5$ nm/ns. To prevent the system from translating due to the adatom impacts on the top surface, the bottom two $(11\bar{2}0)$ planes of the substrate are fixed. To enable the growth to be conducted at a fixed temperature, the two planes of atoms above the fixed region were maintained at a target substrate temperature T. To ensure that the isothermal

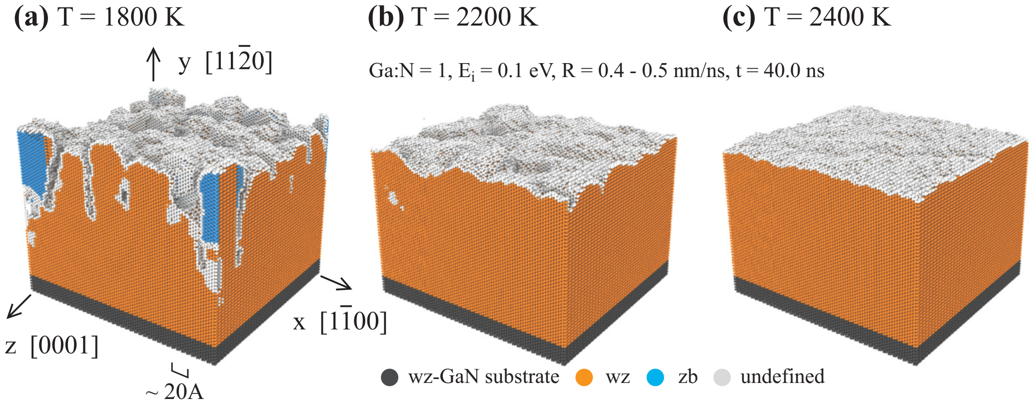

FIG. 1. Simulated GaN films grown on GaN at (a) 1800 K ($T/T_m = 0.50$), (b) 2200 K ($T/T_m = 0.62$), and (c) 2400 K ($T/T_m = 0.67$).

region is not far away from the growth surface and yet does not encompass it, the upper boundary of the isothermal region expands at 85% of the growth rate during simulations. During simulations, some atoms occasionally evaporate from the surface. To maintain the prescribed concentration of the deposition vapor, we placed a repulsive wall well above the free surface to reflect evaporating atoms.

Using this inhomogeneous constant volume, thermostatted algorithm in the MD code LAMMPS [34,35], growth was simulated for 40.0 ns for a matrix of 63 systems involving nine temperatures ($T = 1800, 2000, \ldots, 3400\,\mathrm{K}$) and seven indium contents ($x = 0.0, 0.1, 0.2, 0.3, 0.4, 0.6, 0.8$). Due to the composition dependence of the melt temperature T_m, some films melted at elevated growth temperatures; hence, the analyses presented below are confined to those simulations where solid-phase crystalline growth was obtained using elevated temperatures to minimize kinetic trapping of defects. It is important to note that T_m prescribed by the SW potential is significantly higher than the corresponding experimental values for both GaN and InN [24]. Hence, it is better to relate the simulations to experimental results via the homologous temperature T/T_m. For this purpose, the potential has been used to calculate melting temperature as a function of $\mathrm{In}_x\mathrm{Ga}_{1-x}\mathrm{N}$ composition [24], and the results were well fitted to the mixture rule:

$$T_m(x) = (1 - x)T_{m,\mathrm{GaN}} + xT_{m,\mathrm{InN}}, \tag{1}$$

where $T_{m,\mathrm{GaN}} = 3570\,\mathrm{K}$ and $T_{m,\mathrm{InN}} = 2715\,\mathrm{K}$.

C. Defect analysis methods

The Open Visualization Tool (OVITO) version 2.7.1 [36,37] was used to analyze the MD data and render images of the crystal structure, surface topography, and dislocation-network geometries produced by the simulated growths. This tool enables atomistic characterization of local structure using a common neighbor analysis (CNA) algorithm [38–40], and identification of dislocation lines and their Burgers vectors via the dislocation extraction algorithm (DXA) [36,37]. Both CNA and DXA approaches have been well established. The CNA algorithm is effective in determining the local crystal structure of an atom because the method accounts for three local effects [38–40]: (i) number of neighbor atoms that the central atom and its bonded neighbors have in common, (ii) the total number of bonds between these common neighbors, and (iii) the number of bonds in the longest chain of bonds connecting the common neighbors. The DXA is effective in locating the dislocation lines because it also accounts for three local effects [36,37]: (i) the crystalline and the disordered atoms identified by the CNA method, (ii) the orientable, two-dimensional manifold (referred to as interface mesh) separating the crystalline atoms from the disordered ones, and (iii) continuous local Burgers circuits along this manifold.

III. GaN-ON-GaN HOMOEPITAXIAL GROWTH RESULTS

To provide a reference for comparing the effects of lattice mismatch during growth of heteroepitaxial $\mathrm{In}_x\mathrm{Ga}_{1-x}\mathrm{N}$ films on GaN substrates, we first study the growth of homoepitaxial GaN films on GaN substrates.

A. Structural visualization

As a first step, we examine the structure vs temperature relationships of homoepitaxially grown GaN. The three-dimension (3D) atomic structures of the films obtained after 40.0 ns of deposition at three representative temperatures of 1800, 2200, and 2400 K are shown respectively in Figs. 1(a)–1(c). Here black atoms indicate the initial substrate, orange atoms indicate regions with a local wz configuration, blue atoms indicate zb regions, and white atoms belong neither to wz nor to zb (and hence indicate locally defective or disordered regions such as surfaces, grain boundaries, etc.).

Figure 1 indicates that at a simulated temperature of 1800 K, the film has a rough surface and numerous other defects such as voids and the zb second phase. Interestingly, there are some sharp interfaces between wz and zb phases in Fig. 1(a). This is because these interfaces are parallel to the (0001) plane and the (0001) interfaces are always sharp as discussed previously [24]. At 2200 K, the zb phase is eliminated, the density of voids is reduced, and the free surface becomes much smoother; and, at 2400 K, the surface is essentially flat and other defects are no longer visible. Considering that the local zb domains seen in Fig. 1(a) are defects, all the configurations shown in Fig. 1 exhibit epitaxial growth where the films primarily grow as wz single crystals with the same orientation as the substrate. This is in sharp contrast with the growth in the polar {0001} direction, which produced alternating layers of wz and zb phases [24]. Formation of alternating wz and zb phases occurs during the {0001} growth because the {0001} planes can be stacked either in an ABCABC … sequence of a zb structure, or an ABAB … sequence of a wz structure. Here, however, the $\{11\bar{2}0\}$ planes can only be stacked in an ABAB … wz structure. The observed growth of an epitaxial, single-phase wurtzite-$\mathrm{In}_x\mathrm{Ga}_{1-x}\mathrm{N}$ film on a nonpolar substrate thus enables the analysis of strain relaxation of misfit dislocations by eliminating the presence of partial dislocations that necessarily arise from growth-induced zb phases.

B. Dislocation analysis

The 3D dislocation morphology obtained from OVITO/DXA analysis of the GaN films grown at temperatures of $T =$ 1800, 2000, and 2400 K are shown respectively in Figs. 2(a)–2(c), where the black region represents substrate, the white region corresponds to the surface, and lines are dislocations, which are colored according to Burgers vectors as indicated in the legend.

Figure 2(a) indicates that at the low temperature of 1800 K, numerous dislocations compatible with the structure shown in Fig. 1(a) are formed. Most of the dislocations are in orange corresponding to Shockley partials with a Burgers vector of $b = \langle 1\bar{1}00\rangle/3$. A few dislocations are in green, corresponding to $b = \langle 11\bar{2}0\rangle/3$ perfect dislocations, or in red, corresponding to $b = \langle 2\bar{2}03\rangle/3$. Comparing Fig. 2(a) to Fig. 2(b) indicates that increasing the growth temperature from 1800 to 2000 K reduces the dislocation density significantly. Similarly, Fig. 2(c) shows that increasing the growth temperature further to 2200 K eliminates the dislocations. This is the expected behavior since dislocations are never thermodynamically preferred during homoepitaxy and the elevated temperatures provide the kinetics needed to alleviate the kinetic trapping of dislocations.

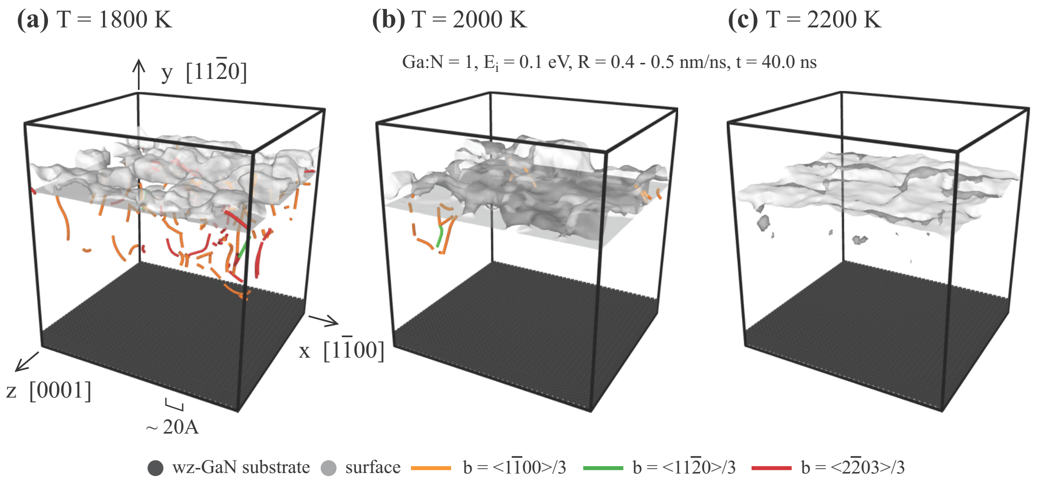

FIG. 2. Dislocation morphology in the GaN films grown on GaN at (a) 1800 K ($T/T_m = 0.50$), (b) 2000 K ($T/T_m = 0.56$), and (c) 2400 K ($T/T_m = 0.67$).

As discussed previously, dislocations should not form when GaN growth occurs homoepitaxially on perfectly flat ($11\bar{2}0$) planes because such a growth pseudomorphically preserves the underlying ABAB… plane stacking sequence of the wz GaN substrate, and the resulting absence of stacking faults also implies the absence of associated partial dislocations. At low temperatures, however, the simulated growth surface becomes rough. As a result, the growth occurs on non-($11\bar{2}0$) planes locally. These non-($11\bar{2}0$) local surfaces can initiate the formation of stacking faults or the zb phase. The peripheries of the stacking faults then become Shockley partial dislocations.

It can be surmised from Figs. 1 and 2 that the defects seen in GaN-on-GaN films grown at low temperatures, such as surface roughness, voids, second phase, and dislocations, are all kinetically trapped because they do not occur at high temperatures. The kinetically trapped defects are likely to be an artifact of the unrealistically high growth rates that must be used in MD simulations; however, since these defects are eliminated at high temperatures, we assume the effects of accelerated growth rates to be effectively mitigated at elevated temperatures such that the simulations are likely to provide representative structures and mechanisms.

IV. In$_x$Ga$_{1-x}$N-ON-GaN HETEROEPITAXIAL GROWTH RESULTS

Having examined the homoepitaxial growth of GaN films on GaN substrates to establish expectations of the elevated temperature and accelerated growth rate simulations, we can now explore the effects of lattice mismatch on the heteroepitaxial growth of In$_x$Ga$_{1-x}$N films on GaN substrates.

A. Structural visualization

The atomic structures of the In$_x$Ga$_{1-x}$N films obtained after 40.0 ns of deposition are shown in Fig. 3 for three representative compositions of $x = 0.2$, 0.4, and 0.6 (left to right) and two temperatures of $T = 2000$ and 2400 K (upper vs lower). Here, again, black atoms indicate the initial substrate, orange atoms are part of a wz structure, blue atoms are part of a zb structure, and white atoms are in defected regions.

Figure 3 indicates that at the low temperature, there exist various defects including surface roughness, voids, and the secondary zb phase. At the high temperature, the defect densities are significantly lower, particularly when indium content is reduced. Clearly, high temperatures eliminate a substantial number of kinetically trapped defects as discussed previously. Despite these defects, overall, the films shown in Fig. 3 can be viewed as single wz crystal with the same orientation as the substrate. Hence, the simulations predict epitaxial growth of In$_x$Ga$_{1-x}$N films on GaN substrates.

B. Dislocation analysis

To analyze the dislocations in the lattice mismatched systems, the 3D dislocation morphology obtained from the In$_x$Ga$_{1-x}$N films grown at a constant temperature of $T = 2600$ K and three different indium contents ($x = 0.2$, 0.4, and 0.6) are shown respectively in Figs. 4(a)–4(c), where again the black region represents substrate, the white region corresponds to the surface, and lines are dislocations with colors indicating Burgers vectors as marked in the legend. Here a higher temperature (2600 K) than those used in Fig. 3 is used to ensure the reduction of nonequilibrium defects in the In$_x$Ga$_{1-x}$N films.

Figure 4(a) indicates that dislocations do not form at the low indium content of $x = 0.2$, and hence implies that the temperature 2600 K is high enough to eliminate kinetically trapped dislocations. On the other hand, Figs. 4(b) and 4(c) show that dislocation density increases as indium content increases above $x = 0.2$. If kinetic trapping is essentially independent of indium content, it follows that the dislocations observed at higher indium content are the consequence of lattice mismatch. Interestingly, Figs. 4(b) and 4(c) show that some dislocations lie approximately on the In$_x$Ga$_{1-x}$N film/GaN substrate interface, whereas other dislocations are threading dislocations extending from the interface all the way to the surface. Specifically, Fig. 4(c) clearly shows that on the interface, there are two roughly perpendicular arrays of dislocations: one array is in red where the dislocation-line directions are parallel to [$1\bar{1}00$] (the x axis) and one array is in green where the line

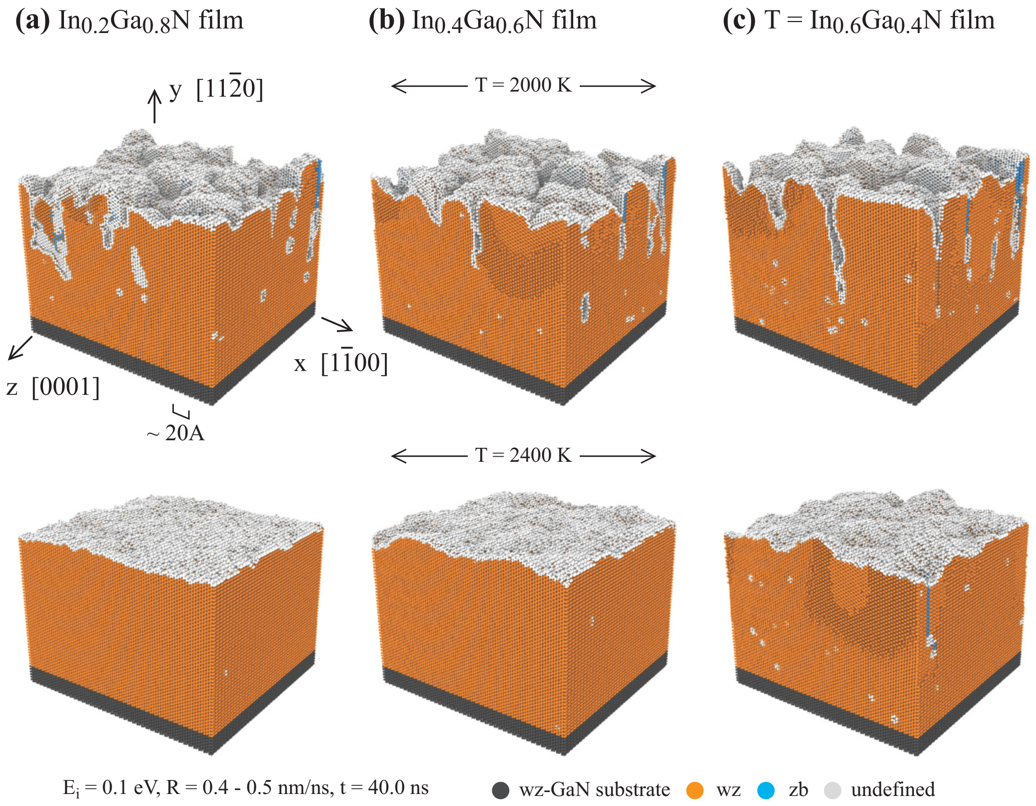

FIG. 3. $\mathrm{In}_x\mathrm{Ga}_{1-x}\mathrm{N}$ films grown on GaN at three compositions of (a) $x = 0.2$, (b) $x = 0.4$, and (c) $x = 0.6$ and two temperatures of $T = 2000$ K (top row) and $T = 2400$ K (bottom row).

directions are parallel to [0001] (the z axis). Furthermore, the interfacial dislocations parallel to [0001] have a Burgers vector $b = \langle 11\bar{2}0\rangle/3$ that is perpendicular to $\langle 0001\rangle$. Hence, these dislocations are purely edge dislocations. As a special case of the $\langle 11\bar{2}0\rangle/3$ family, $[2\bar{1}\bar{1}0]/3$ has a component parallel to $[1\bar{1}00]$. Hence, the $\langle 11\bar{2}0\rangle/3$ dislocations can release lattice mismatch strain along x-$[1\bar{1}00]$. Similarly, the dislocations parallel to $[1\bar{1}00]$ have a Burgers vector $b = \langle 2\bar{2}03\rangle/3$. Such a Burgers vector has a component parallel to $\langle 0001\rangle$. Hence, the $\langle 2\bar{2}03\rangle/3$ dislocations can release the lattice mismatch strain along z-[0001].

Figures 4(b) and 4(c) also show, for the simulated systems, that misfit dislocations are always accompanied by threading dislocations. This is in good agreement with the experimental observation on $\mathrm{In}_x\mathrm{Ga}_{1-x}\mathrm{N}$-on-GaN films that interfacial misfit dislocations are accompanied by threading dislocations [41]. Interestingly, some previous work [41] assumed that the interfacial misfit dislocations are formed via the bending of pre-existing threading dislocations in the substrate. Our MD results indicate that the pre-existing threading dislocations are not required for misfit dislocation formation. In addition, the detailed 3D dislocation morphology revealed by the MD

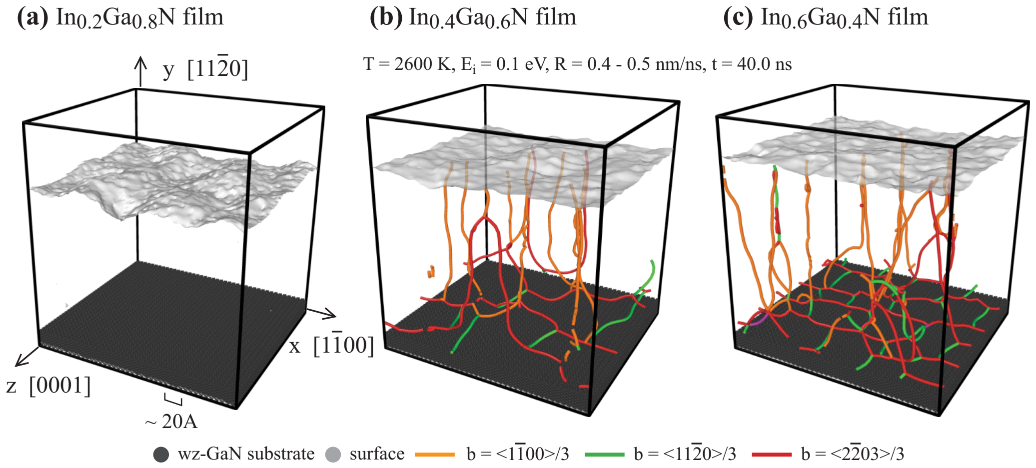

FIG. 4. Dislocation morphology in the $\mathrm{In}_x\mathrm{Ga}_{1-x}\mathrm{N}$ films grown on GaN at a temperature of 2600 K for three indium contents: (a) $x = 0.2$ ($T/T_m = 0.76$), (b) $x = 0.4$ ($T/T_m = 0.81$), and (c) $x = 0.6$ ($T/T_m = 0.85$).

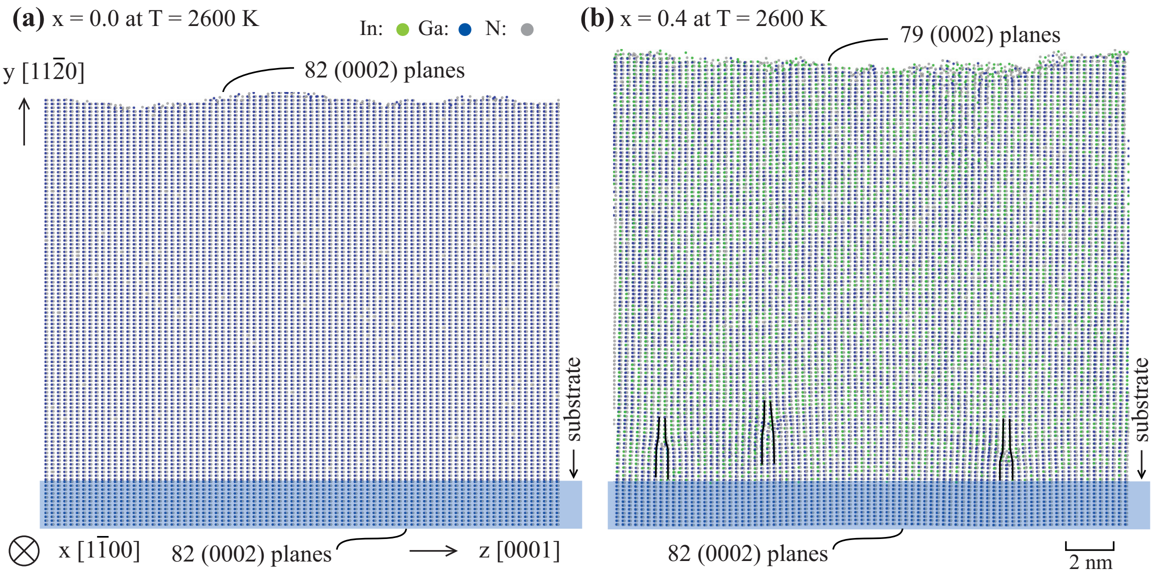

FIG. 5. Visualization of misfit dislocations in $In_xGa_{1-x}N$ films grown at an MD temperature of 2600 K. (a) $x = 0.0$ ($T/T_m = 0.73$), and (b) $x = 0.4$ ($T/T_m = 0.81$). Crystallographic orientation is marked in (a).

simulations allows experimentalists to explore strategies to change the relative fraction of threading vs interfacial dislocations in the future. This is important because threading dislocations are detrimental since they pass through the entire active region of device grown epitaxially on top of the heterolayer.

Lastly, following our examination of kinetic trapping, we investigate the thermodynamic stability of the dislocation network by annealing one of the films ($In_{0.3}Ga_{0.7}N$ film grown on GaN) for 40 ns at 2600 K. Despite a few dislocation loops disappearing and some changes in the surface topography, the overall network structure and topology is essentially unchanged. This thermal stability gives us further confidence that the structures formed are not artifacts of the high deposition rate.

C. Virtual microscopy of misfit dislocations

Compared with the two-dimensional (2D) images of misfit dislocations obtained from high resolution transmission electron microscopy (HRTEM), Figs. 2 and 4 have significant advantages as they provide detailed 3D information on dislocation morphology. To directly relate simulations to experimental data, however, we can also examine 2D projections of selected local slabs, excised from the MD-grown film, in a way like HRTEM. Using this approach, y-z cross-sectional views of the films grown at $T = 2600\,\mathrm{K}$ are shown in Fig. 5(a) for a homoepitaxial GaN-on-GaN film ($T/T_m = 0.73$) and in Fig. 5(b) for a heteroepitaxial $In_{0.4}Ga_{0.6}N$-on-GaN film ($T/T_m = 0.81$). It can be seen from Fig. 5(a) that along the z direction (horizontal axis), there are 82 (0002) planes in the substrate at the bottom and there are exactly 82 such planes on the top surface. Hence, no misfit dislocations are created during the homoepitaxial growth of GaN on GaN as we expect. On the other hand, Fig. 5(b) indicates that there are only 79 (0002) planes on the top surface as compared with the 82 (0002) planes in the substrate. This means that three misfit dislocations with a Burgers vector component in the [0001] direction are created during the heteroepitaxial growth of this $In_xGa_{1-x}N$ film. This results in a relatively high dislocation density with an average dislocation spacing in Fig. 5(b) around 7 nm. The associated lattice constants are $c_{\mathrm{GaN}} = 5.254$ Å (substrate) and $c_{\mathrm{In0.4Ga0.6N}} = 5.478$ Å (film) [24]. Along the z direction, the lattice mismatch for this $In_{0.4}Ga_{0.6}N$-on-GaN film without dislocations is therefore $(c_{\mathrm{GaN}} - c_{\mathrm{In0.4Ga0.6N}})/c_{\mathrm{In0.4Ga0.6N}} = -0.041$. With three dislocations, the dimension of a free film is $79\,c_{\mathrm{In0.2Ga0.8N}}/2$. The dimension of substrate is $82c_{\mathrm{GaN}}/2$. Hence, the lattice mismatch becomes $(82c_{\mathrm{GaN}} - 79c_{\mathrm{In0.4Ga0.6N}})/(79c_{\mathrm{In0.4Ga0.6N}}) = -0.004$. This means that the three dislocations reduced the lattice mismatch by one order of magnitude.

The same analysis was applied on the x-y projection for the two configurations shown in Fig. 5. As expected, we again found no misfit dislocations for the GaN-on-GaN case. On the other hand, in the $In_{0.4}Ga_{0.6}N$-on-GaN film we found two misfit dislocations of a Burgers vector of $b = \langle 11\bar{2}0\rangle/3$, which result in four missing $(1\bar{1}00)$ planes along $[1\bar{1}00]$ that has a total of 84 $(1\bar{1}00)$ planes. The dislocation spacing along this direction is about 12 nm. The lattice constant $a_{\mathrm{GaN}} = 3.220$ Å and $a_{\mathrm{In0.4Ga0.6N}} = 3.357$ Å [24]. Along the x direction, the lattice mismatch without and with dislocations are therefore $(3.220 - 3.361)/3.361 = -0.042$ and $(84a_{\mathrm{GaN}} - 80a_{\mathrm{In0.4Ga0.6N}})/(80\,a_{\mathrm{In0.4Ga0.6N}}) = 0.007$.

D. Analysis of the as-grown stress/strain

To obtain the film stress for nominally 16 nm thick films grown at 2600 K, the in-plane stresses are averaged over the entire film defined by the region between the substrate-film boundary and the free surface minus any amorphous/rough surface layer; isothermal, constant volume dynamics are used to obtain the said averages. The calculated stresses are shown in Fig. 6(a) as a function of indium content for the entire simulated growth, and in Fig. 6(b) as a function of film thickness for a single film at a given indium content $x_{\mathrm{In}} = 0.4$ at various stages

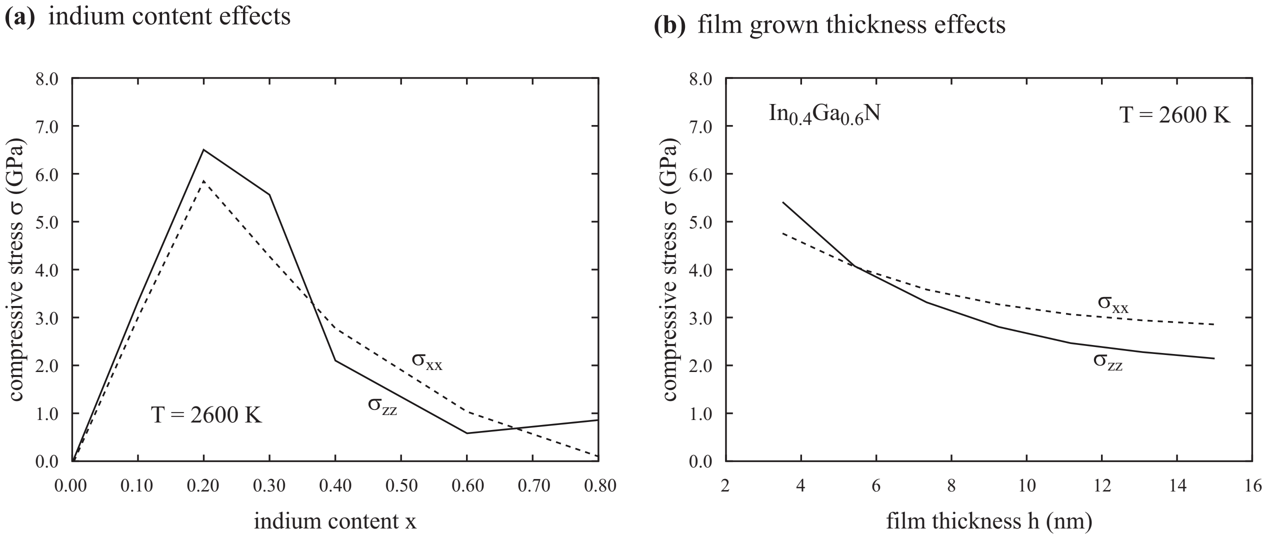

FIG. 6. *In situ*, in-plane stresses of $\mathrm{In}_x\mathrm{Ga}_{1-x}\mathrm{N}$ film at a temperature of 2600 K. (a) Effects of indium content x_{In} at a fixed film thickness of 16 nm, and (b) effects of grown film thickness h for a fixed indium content $x_{\mathrm{In}} = 0.4$.

of growth. As can be seen in Fig. 6(a) the stress is zero for GaN-on-GaN growth, and highest and nearly equal in the two in-plane directions at indium content $x_{\mathrm{In}} = 0.2$. At $x_{\mathrm{In}} = 0.2$, the film remains essentially coherent and dislocation-free as can be seen in Fig. 4(a). Then, after the formation of the dislocation networks for $x_{\mathrm{In}} > 0.2$, the in-plane film stress relaxes with increasing indium content and the two in-plane stresses deviate from each other due to nonuniformity in the networks. Focusing on the growth of the $x_{\mathrm{In}} = 0.4$ film, Fig. 6(b) implies that the average film stress is highest for the initial growth and decreases with thickness.

To obtain the elastic misfit strain, we cleaved the same heteroepitaxially grown films from their substrates and removed any amorphous surface layers. We then used time-averaged MD to relax the resulting laterally periodic systems to zero stress with zero pressure isobaric, isothermal dynamics. The final, averaged box dimensions are taken as the equilibrium film size l_0, and strain is calculated along the x and z axes, relative to the corresponding initial simulation box dimension l_f as $\varepsilon = \frac{l_f - l_0}{l_0}$. The calculated strains are shown in Fig. 7(a) as a function of indium content at the full calculated film thickness, and in Fig. 7(b) as a function of film grown thickness for a fixed indium content of $x_{\mathrm{In}} = 0.4$.

Lateral compressive strains were obtained in Fig. 7(a), as expected for $\mathrm{In}_x\mathrm{Ga}_{1-x}\mathrm{N}$ films given the initial pseudomorphic coherency to GaN. It can be inferred from Fig. 7(a) that the elastic strain is highest at $x_{\mathrm{In}} = 0.2$, where the film remains essentially dislocation-free. For $x_{\mathrm{In}} > 0.2$, increasing indium content induces the formation of misfit dislocations to relieve the strain in the film, and thus the strain is reduced. It is clear from comparing Fig. 7(a) to Fig. 6(a) that the recovered strain is mainly elastic, i.e., the strain correlates well stress. As can

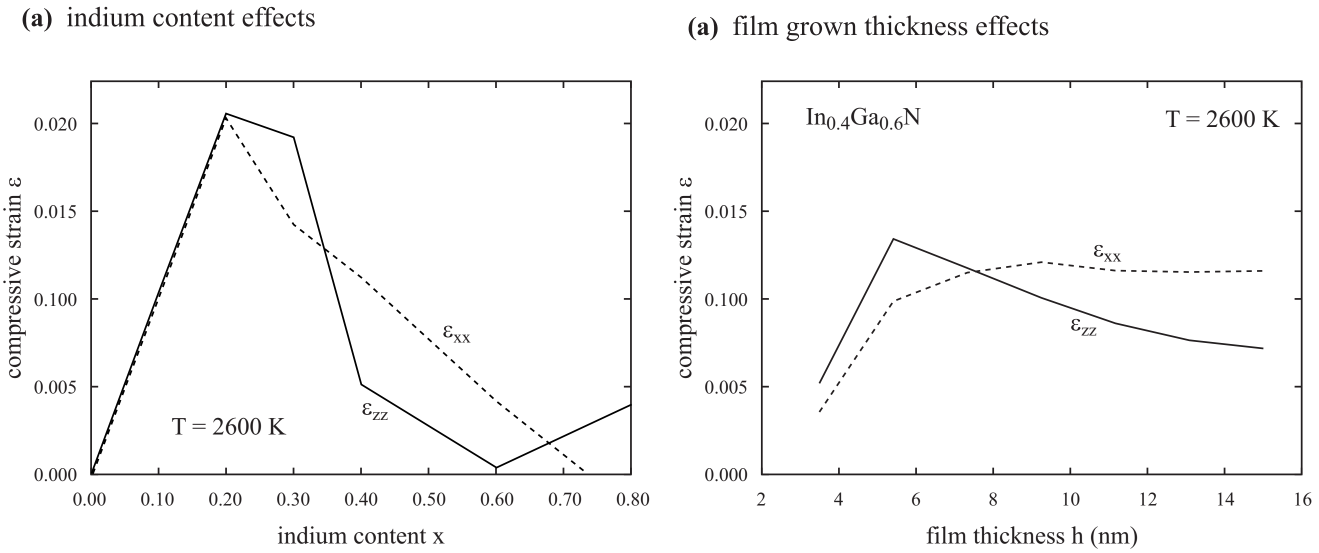

FIG. 7. Elastic strain in $\mathrm{In}_x\mathrm{Ga}_{1-x}\mathrm{N}$ films grown at a temperature of 2600 K. (a) Effects of indium content x_{In} at a fixed film thickness of 16 nm, and (b) effects of grown film thickness h for a fixed indium content $x_{\mathrm{In}} = 0.4$.

be seen from Fig. 7(b), the largest compressive strain occurs in the 5–9 nm thickness range. As the film grows past this critical thickness, misfit dislocations form, which relieves elastic strain in the layer and the strain averaged over the film becomes less compressive. Further examination of the formation of the dislocations will be given in the next section.

V. DISCUSSION

A. Critical thickness analysis

As the film thickness increases above a critical value, the strain energy becomes larger than the energy to nucleate misfit dislocations. As a result, misfit dislocations are formed to release the misfit strain energy [42]. To determine the critical thickness of misfit dislocation formation in the $In_xGa_{1-x}N$-on-GaN films, dislocation density (total dislocation length per unit of volume) was calculated as a function of MD-simulated grown thickness for six samples with different indium contents of $x = 0.1$, 0.2, 0.3, 0.4, 0.6, and 0.8, obtained at the same growth temperature of 2600 K. The results are shown in Fig. 8.

Figure 8 indicates that, roughly, the critical thickness h_c is above 14 nm for the $x_{\mathrm{In}} = 0.1$, 0.2 films, about 7 nm for the $x_{\mathrm{In}} = 0.3$ film, and in the range 2–4 nm for the other films with $x_{\mathrm{In}} \geqslant 0.4$. Evaluation of the Matthews-Blakeslee critical thickness model [43] with an isotropic approximation for Poisson's ratio [18] using the elastic constants of the SW potential yields: $h_c \sim 10.3$, 3.4, and 1.1 nm for $x_{\mathrm{In}} = 0.1$, 0.2, and 0.3, respectively, for dislocations with Burgers vectors $b = \langle 1\bar{1}00\rangle/3$ and $b = \langle 11\bar{2}0\rangle/3$, and $h_c \sim 40.9$, 14.9, and 7.1 nm for dislocations with Burgers vector $b = \langle 2\bar{2}03\rangle/3$. The values calculated by Holec *et al.* [44] are $h_c \sim 8.7$, 3.4, and 1.6 nm for $x_{\mathrm{In}} = 0.1$, 0.2, and 0.3, respectively. This level of correspondence is acceptable given that the literature misfit-dislocation critical-thickness models [44] are based on equilibrium continuum-elasticity-theory force-balance (or energy-balance) for glissile propagation of a single, pre-existing dislocation. Such models do not include additional complexities such as nucleation kinetics, multiple-dislocation interactions, and other nonequilibrium growth phenomena that likely cause our MD simulations of misfit introduction to differ from the traditional equilibrium critical thickness. Notably, dislocation nucleation mechanisms seen in our simulations are separately discussed below.

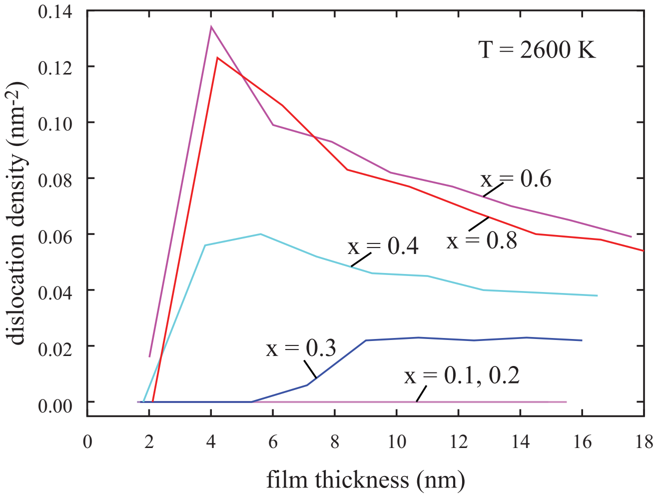

FIG. 8. Dislocation density as a function of grown film thickness for six $In_xGa_{1-x}N$-on-GaN samples with different indium contents of $x = 0.1$, 0.2, 0.3, 0.4, 0.6, and 0.8, obtained at the same growth temperature of $T = 2600$ K ($T/T_m = 0.75, 0.76, 0.78, 0.81, 0.85$, and 0.90, respectively).

B. Misfit dislocation formation mechanisms

Figures 4 and 5 indicate that misfit and threading dislocations are created during heteroepitaxial growth of $In_xGa_{1-x}N$ on dislocation-free GaN substrates. We now use MD to identify detailed mechanisms of dislocation nucleation.

1. *Time series observation*

For the same z-y projection of the $In_{0.4}Ga_{0.6}N$ film grown at 2600 K as shown in Fig. 5(b), time-resolved series images are displayed in Figs. 9(a)–9(d) to examine the local region that will later contain the misfit dislocation identified at far right in Fig. 5(b). Here again the black region represents the substrate, white atoms are at the surface, orange and blue atoms distinguish wz and zb structures, dislocations are marked by thick lines with colors indicating Burgers vectors, and the extra planes are revealed by thin black lines.

It can be seen from Fig. 9(a) that at time $t = 7.2$ ns there is no dislocation in the film but a surface depression has formed with an attendant disordered near-surface region. At time $t = 7.6$ ns [Fig. 9(b)] this surface defect has expanded and exhibits a "V" shape which 3D analysis indicates to be a surface pit. By time $t = 8.0$ ns, a dislocation with a Burgers vector of $b = \langle 2\bar{2}03\rangle/3$ has been nucleated in this defective region [Fig. 9(c)]. This Burgers vector has a component in the z axis, and hence is a misfit dislocation that can release the strain energy in the z direction. Indeed, we can see that in the projected image, this dislocation creates an extra half (0002) plane below the dislocation core as shown by the thin black lines. Figure 9(d) confirms that this dislocation is buried by new adatoms by 8.4 ns and remains at a fixed location relative to the substrate. 3D analysis indicated that this dislocation is in fact a half dislocation loop with two ends terminating at the surface (note that the dislocation lines extending into and out of the slab shown have been clipped in this visualization).

While misfit dislocations may at times form by bending the pre-existing threading dislocations [41], we see herein that when initial threads are absent, misfit dislocations are nucleated at the surface, with preferential locations at surface pits. The geometric requirement for the formation of misfit dislocations is that their two ends must terminate at the surface. Hence, misfit dislocations are always connected to threading dislocations. We observe that as the misfit dislocation extends, the two threading dislocations continue to move apart. Another unique observation here is that once nucleated at the surface, misfit dislocations do not necessarily migrate towards the interface as proposed in previous models [43,44]. Instead, they can be buried into the film by later deposited atoms. This is important because the migration towards the interface requires that the misfit dislocation has a Burgers vector component parallel to the growth direction. Not all misfit dislocations satisfy this condition as the only requirement for misfit dislocations is that they have a Burger vector component parallel to the surface. For

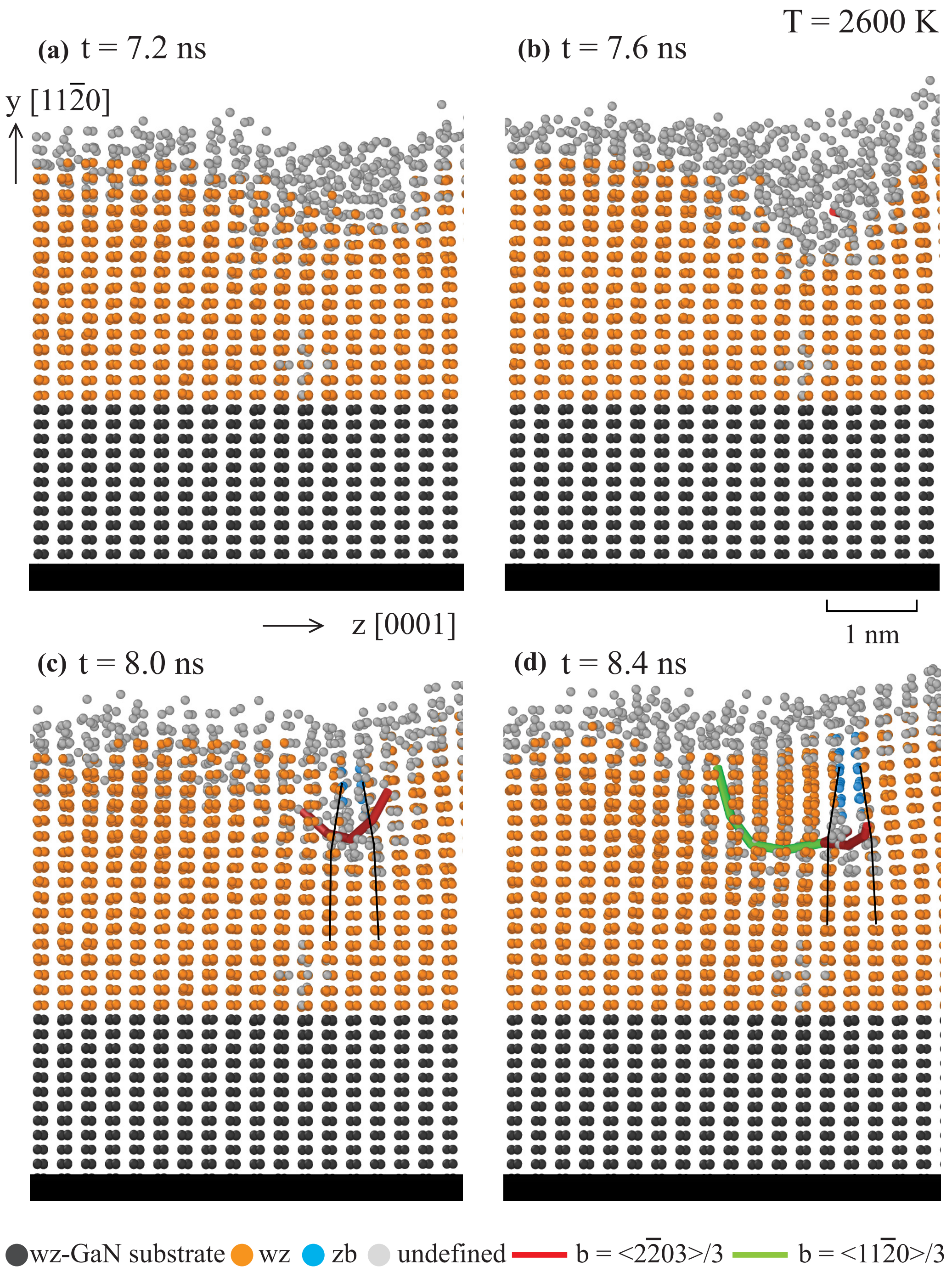

FIG. 9. Time series images showing dislocation formation mechanisms during growth of $In_{0.4}Ga_{0.6}N$ film at 2600 K ($T/T_m = 0.81$). (a) $t = 7.2$ ns, (b) $t = 7.6$ ns, (c) $t = 8.0$ ns, and (d) $t = 8.4$ ns. Only a 1.2 nm section of the system is shown for clarity and dislocation lines extending into and out of the visible section have been clipped.

example, the Burgers vector $[2\bar{2}03]/3$ is perpendicular to the growth direction $[11\bar{2}0]$. On the other hand, it should be noted dislocations can still climb to the interface through diffusion. This diffusion mechanism, however, may not be captured by the short time frame of MD simulations.

It should also be noted that the misfit dislocations observed in Fig. 9 appear to be a distance away from the interface. This is an illusion of both the small spatial scale used in Fig. 9 and the early stage of the film growth at which nucleation occurs. Using a larger scale at a later time, as in Fig. 5(b), we see that these misfit dislocations are actually fairly close to the interface.

2. *Surface pit formation*

To further understand dislocation morphology in 3D, we analyze in detail the final configuration of the $In_{0.8}Ga_{0.2}N$ film grown at 2400 K. Figure 10(a) shows 3D morphology of various defects in the film. The two ends of misfit dislocations on the $In_{0.8}Ga_{0.2}N$/GaN interfacial plane (mostly red and green lines) can normally be traced to a pair of threading dislocations

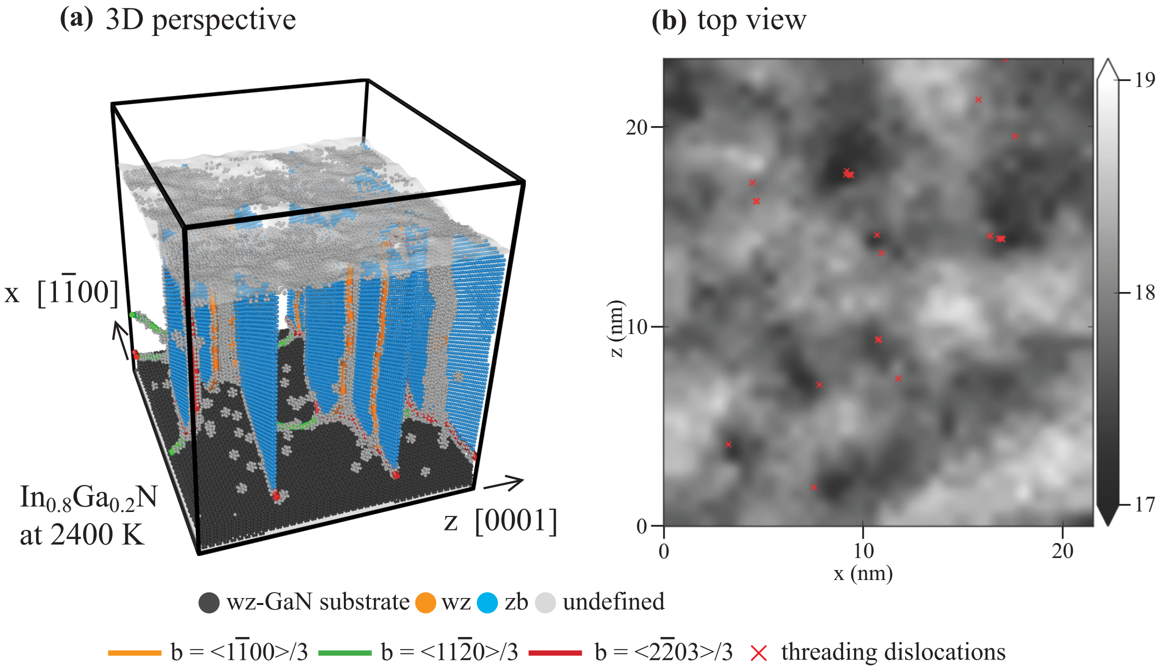

FIG. 10. Correspondence of surface pits and threading dislocations in $In_{0.8}Ga_{0.2}N$ at 2400 K ($T/T_m = 0.83$): (a) 3D view and (b) top view. In (b), the gray-tone scale represents the film height in nanometers.

(orange lines) that run from the interface to the surface. Whenever a pair of threading dislocations connect via an interfacial misfit dislocation segment with Burgers vector $b = \langle 2\bar{2}03\rangle/3$, a single-plane zb stacking fault is formed. This fault is of course due to the missing plane of *c*-plane atoms resulting from the misfit dislocation's propagation (and not due to direct nucleation and growth of the zb phase, as one might see for growth on singular polar surfaces [24]). Obviously when these two threading dislocations move apart, the width of the stacking fault plane and the length of the misfit dislocation increase.

Figure 10(b) shows a top view of the surface profile of the same $In_{0.8}Ga_{0.2}N$ film where dark areas represent surface valleys and bright areas represent surface peaks, and threading dislocations are indicated by the red "×". Interestingly, many threading dislocations are seen to coincide with surface valleys. Threading dislocations migrate after they are nucleated as discussed above; however, the statistically significant correlation between threading dislocations and surface pits is interesting, and seems to be consistent with the observation in Fig. 9 that dislocations tend to nucleate at the positions of the "V" surface defects.

Finally, we did not observe deepening of the surface pits once they were formed. This suggests that there is no significant deviation from the average growth rate near the pit regions over the remaining course of the simulation—once the pit has formed.

VI. CONCLUSION

Extensive large-scale molecular dynamics vapor deposition simulations have been performed to study heteroepitaxial growth of $In_xGa_{1-x}N$ films on nonpolar (11$\bar{2}$0) GaN surfaces, in a composition range of $0.0 \leqslant x \leqslant 0.8$ with the homologous temperature above half the melt temperature. A composition-dependent temperature range was discovered where the films predominantly contain thermodynamically driven misfit and associated threading dislocations, whereas the other kinetically trapped dislocation segments have been effectively eliminated. The existence of this temperature range indicates that we have mitigated the artificial kinetic trapping of dislocations associated with accelerated growth rate that is necessary in MD simulations. Analysis of the MD results within this temperature range resulted in the following conclusions:

(1) Growth on the nonpolar (11$\bar{2}$0) GaN surfaces eliminates polymorphisms (alternating wz and zb phases) because (11$\bar{2}$0) reveals the intrinsic ABAB... basal-plane stacking sequence of the wurtzite substrate at the growth surface; subsequent pseudomorphic growth thus prevents formation of the zb ABCABC... sequence.

(2) Misfit dislocations exhibit two perpendicular arrays on the $In_xGa_{1-x}N$-on-GaN interface that are parallel respectively to $\langle 1\bar{1}00\rangle$ and $\langle 0001\rangle$ directions. These two arrays have Burgers vector families $b = \langle 2\bar{2}03\rangle/3$ and $b = \langle 11\bar{2}0\rangle/3$, respectively, which can effectively release the 2D lattice mismatch strain energy on the interfacial plane. As expected, misfit dislocations exhibit 3D network morphology wherein the misfit segments are always connected to threading dislocations that reach the surface.

(3) The critical film thickness for misfit-dislocation formation in our MD-grown $In_xGa_{1-x}N$-on-GaN heterostructures is above 14 nm for $x_{In} \leqslant 0.2$, about 7 nm for $x_{In} = 0.3$, and around 2–4 nm for $0.4 \leqslant x_{In} \leqslant 0.8$, in rough agreement with previous continuum-elasticity-theory calculations. Unlike the previously proposed models, however, misfit dislocations do not necessarily migrate towards the interface once then are nucleated at the surface.

(4) Most importantly, through use of MD growths, the nucleation of misfit dislocation half loops has been observed

at the atomistic level. The nucleation is observed to occur at sites of V-shaped nanopits that arise on the growing surface.

ACKNOWLEDGMENTS

Sandia National Laboratories is a multimission laboratory managed and operated by National Technology and Engineering Solutions of Sandia, LLC., a wholly owned subsidiary of Honeywell International, Inc., for the U.S. Department of Energy's National Nuclear Security Administration under contract DE-NA-0003525. This work is supported by Sandia's Laboratory Directed Research and Development (LDRD) program.

---

[1] E. F. Schubert, J. K. Kim, H. Luo, and J. Q. Xi, Solid-state lighting—A benevolent technology, Rep. Prog. Phys. **69**, 3069 (2006).

[2] M. S. Shur and A. Zukauskas, Solid-state lighting: Toward superior illumination, Proc. IEEE **93**, 1691 (2005).

[3] A. Bergh, G. Craford, A. Duggal, and R. Haitz, The promise and challenge of solid-state lighting, Phys. Today **54**, 42 (2001).

[4] J. Y. Tsao, Solid-state lighting—Lamps, chips, and materials for tomorrow, IEEE Cir. Dev. Mag. **20**, 28 (2004).

[5] D. A. Steigerwald, J. C. Bhat, D. Collins, R. M. Fletcher, M. O. Holcomb, M. J. Ludowise, P. S. Martin, and S. L. Rudaz, Illumination with solid state lighting technology, J. Sel. Top. Quantum Electron. **8**, 310 (2002).

[6] M. R. Krames, O. B. Shchekin, R. Mueller-Mach, G. O. Mueller, L. Zhou, G. Harbers, and M. G. Craford, Status and future of high-power light-emitting diodes for solid-state lighting, J. Display Tech. **3**, 160 (2007).

[7] Z. Deng, Y. Jiang, Z. Ma, W. Wang, H. Jia, J. Zhou, and H. Chen, A novel wavelength-adjusting method in InGaN-based light-emitting diodes, Sci. Rep. **3**, 3389 (2013).

[8] J. Wu, When group-III nitrides go infrared: New properties and perspectives, J. Appl. Phys. **106**, 011101 (2009).

[9] J. M. Phillips, M. E. Coltrin, M. H. Crawford, A. J. Fischer, M. R. Krames, R. Muller-Mach, G. O. Mueller, Y. Ohno, L. E. S. Rohwer, J. A. Simmons, and J. Y. Tsao, Research challenges to ultra-efficient inorganic solid-state lighting, Laser Photon. Rev. **1**, 307 (2007).

[10] W. Feng, V. V. Kuryatkov, A. Chandolu, D. Y. Song, M. Pandikunta, S. A. Nikishin, and M. Holtz, Green light emission from InGaN multiple quantum wells grown on GaN pyramidal stripes using selective area epitaxy, J. Appl. Phys. **104**, 103530 (2008).

[11] H. P. Zhao, G. Y. Liu, X. H. Li, R. A. Arif, G. S. Huang, J. D. Poplawsky, S. T. Penn, V. Dierolf, and N. Tansu, Design and characteristics of staggered InGaN quantum-well light-emitting diodes in the green spectral regime, IET Optoelectron. **3**, 283 (2009).

[12] H. P. Zhao, G. Y. Liu, J. Zhang, J. D. Poplawsky, V. Dierolf, and N. Tansu, Approaches for high internal quantum efficiency green InGaN light-emitting diodes with large overlap quantum wells, Opt. Express A **19**, 991 (2011).

[13] Z. Liliental-Weber, M. Benamara, J. Washburn, J. Z. Domagala, J. Bak-Misiuk, E. L. Piner, J. C. Roberts, and S. M. Bedair, Relaxation of InGaN thin layers observed by x-ray and transmission electron microscopy studies, J. Electron. Mater. **30**, 439 (2001).

[14] T. L. Song, Strain relaxation due to V-pit formation in $In_xGa_{1-x}N$/GaN epilayers grown on sapphire, J. Appl. Phys. **98**, 084906 (2005).

[15] W. Lu, D. B. Li, C. R. Li, and Z. Zhang, Generation and behavior of pure-edge threading misfit dislocations in $In_xGa_{1-x}N$/GaN multiple quantum wells, J. Appl. Phys. **96**, 5267 (2004).

[16] S. Pereira, On the Interpretation of structural and light emitting properties of InGaN/GaN epitaxial layers grown above and below the critical layer thickness, Thin Solid Films **515**, 164 (2006).

[17] J. W. Matthews and A. E. Blakeslee, Defects in epitaxial multilayers: I. Misfit dislocations, J. Cryst. Growth **27**, 118 (1974).

[18] A. E. Romanov, E. C. Young, F. Wu, A. Tyagi, C. S. Gallinat, S. Nakamura, S. P. DenBaars, and J. S. Speck, Basal plane misfit dislocations and stress relaxation in III-nitride semipolar heteroepitaxy, J. Appl. Phys. **109**, 103522 (2011).

[19] R. Liu, J. Mei, S. Srinivasan, F. A. Ponce, H. Omiya, Y. Narukawa, and T. Mukai, Generation of misfit dislocations by basal-plane slip in InGaN/GaN heterostructures, Appl. Phys. Lett. **89**, 201911 (2006).

[20] B. Jahnen, M. Albrecht, W. Dorsch, S. Christiansen, H. P. Strunk, D. Hanser, and R. F. Davis, Pinholes, dislocations and strain relaxation in InGaN, MRS Internet J. Nitride Semicond. Res. **3**, 39 (1998).

[21] R. Liu, J. Mei, S. Srinivasan, H. Omiya, F. A. Ponce, D. Cherns, Y. Narukawa, and T. Mukai, Misfit dislocation generation in InGaN epilayers on free-standing GaN, Jpn. J. Appl. Phys. **45**, L549 (2006).

[22] D. Iida, Y. Kondo, M. Sowa, T. Sugiyama, M. Iwaya, T. Takeuchi, S. Kamiyama, and I. Akasaki, Analysis of strain relaxation process in GaInN/GaN heterostructure by in situ x-ray diffraction monitoring during metalorganic vapor-phase epitaxial growth, Phys. Status Solidi-Rapid Res. Lett. **7**, 211 (2013).

[23] S. Srinivasan, L. Geng, R. Liu, F. A. Ponce, Y. Narukawa, and S. Tanaka, Slip systems and misfit dislocations in InGaN epilayers, Appl. Phys. Lett. **83**, 5187 (2003).

[24] J. Gruber, X. W. Zhou, R. E. Jones, S. R. Lee, and G. J. Tucker, Molecular dynamics studies of defect formation during heteroepitaxial growth of InGaN alloys on (0001) GaN surfaces, J. Appl. Phys. **121**, 195301 (2017).

[25] F. H. Stillinger and T. A. Weber, Computer-simulation of local order in condensed phases of silicon, Phys. Rev. B **31**, 5262 (1985).

[26] X. W. Zhou and R. E. Jones, A Stillinger-Weber potential for InGaN, J. Mater. Sci. Res. **6**, 88 (2017).

[27] X. W. Zhou, R. E. Jones, and J. Gruber, Molecular dynamics simulations of substitutional diffusion, Comput. Mater. Sci. **128**, 331 (2017).

[28] X. W. Zhou, D. K. Ward, and M. E. Foster, An analytical bond-order potential for the aluminum copper binary system, J. Alloys Compounds **680**, 752 (2016).

[29] C.-Y. Yeh, Z. W. Lu, S. Froyen, and A. Zunger, Zinc-blende-wurtzite polytypism in semiconductors, Phys. Rev. B **46**, 10086 (1992).

[30] X. W. Zhou, D. K. Ward, J. A. Zimmerman, J. L. Cruz-Campa, D. Zubia, J. E. Martin, and F. van Swol, An atomistically validated continuum model for strain relaxation and misfit dislocation formation, J. Mech. Phys. Solids **91**, 265 (2016).

[31] X. W. Zhou, R. B. Sills, D. K. Ward, and R. A. Karnesky, Atomistic calculations of dislocation core energy in aluminium, Phys. Rev. B **95**, 054112 (2017).

[32] J. Elsner, R. Jones, P. K. Sitch, V. D. Porezag, M. Elstner, T. Frauenheim, M. I. Heggie, S. Öberg, and P. R. Briddon, Theory of Threading Edge and Screw Dislocations in GaN, Phys. Rev. Lett. **79**, 3672 (1997).

[33] A. Béré and A. Serra, Atomic structure of dislocation cores in GaN, Phys. Rev. B **65**, 205323 (2002).

[34] S. Plimpton, Fast parallel algorithms for short-range molecular dynamics, J. Comput. Phys. **117**, 1 (1995).

[35] lammps.sandia.gov.

[36] A. Stukowski and K. Albe, Extracting dislocations and non-dislocation crystal defects from atomistic simulation data, Model. Simul. Mater. Sci. Eng. **18**, 085001 (2010).

[37] A. Stukowski, V. V. Bulatov, and A. Arsenlis, Automated identification and indexing of dislocations in crystal interfaces, Model. Simul. Mater. Sci. Eng. **20**, 085007 (2012).

[38] J. D. Honeycutt and H. C. Andersen, Molecular dynamics study of melting and freezing of small Lennard-Jones clusters, J. Phys. Chem. **91**, 4950 (1987).

[39] D. Faken and H. Jonsson, Systematic analysis of local atomic structure combined with 3D computer graphics, Comput. Mater. Sci. **2**, 279 (1994).

[40] A. Stukowski, Structure identification methods for atomistic simulations of crystalline materials, Model. Simul. Mater. Sci. Eng. **20**, 045021 (2012).

[41] P. S. Hsu, E. C. Young, A. E. Romanov, K. Fujito, S. P. DenBaars, S. Nakamura, and J. S. Speck, Misfit dislocation formation via pre-existing threading dislocation glide in $(11\bar{2}2)$ semipolar heteroepitaxy, Appl. Phys. Lett. **99**, 081912 (2011).

[42] W. D. Nix, Mechanical-properties of thin-films, Metal. Trans. A **20**, 2217 (1989).

[43] L. B. Freund and S. Suresh, *Thin Film Materials: Stress, Defect Formation and Surface Evolution* (Cambridge University Press, Cambridge, 2004).

[44] D. Holec, P. M. F. J. Costa, M. J. Kappers, and C. J. Humphreys, Critical thickness calculations for InGaN/GaN, J. Crystal Growth **303**, 314 (2007).